(article starts on next page)

Epitaxy of GaSe Coupled to Graphene: From In Situ Band Engineering to Photon Sensing

Jonathan Bradford, Benjamin T. Dewes, Mustaqeem Shiffa, Nathan D. Cottam,
Kazi Rahman, Tin S. Cheng, Sergei V. Novikov, Oleg Makarovsky, James N. O'Shea,
Peter H. Beton, Samuel Lara-Avila, Jordan Harknett, Mark T. Greenaway,
and Amalia Patanè*

2D semiconductors can drive advances in quantum science and technologies. However, they should be free of any contamination; also, the crystallographic ordering and coupling of adjacent layers and their electronic properties should be well-controlled, tunable, and scalable. Here, these challenges are addressed by a new approach, which combines molecular beam epitaxy and in situ band engineering in ultra-high vacuum of semiconducting gallium selenide (GaSe) on graphene. In situ studies by electron diffraction, scanning probe microscopy, and angle-resolved photoelectron spectroscopy reveal that atomically-thin layers of GaSe align in the layer plane with the underlying lattice of graphene. The GaSe/graphene heterostructure, referred to as 2semgraphene, features a centrosymmetric (group symmetry D_{3d}) polymorph of GaSe, a charge dipole at the GaSe/graphene interface, and a band structure tunable by the layer thickness. The newly-developed, scalable 2semgraphene is used in optical sensors that exploit the photoactive GaSe layer and the built-in potential at its interface with the graphene channel. This proof of concept has the potential for further advances and device architectures that exploit 2semgraphene as a functional building block.

J. Bradford, B. T. Dewes, M. Shiffa, N. D. Cottam, K. Rahman, T. S. Cheng,
S. V. Novikov, O. Makarovsky, J. N. O'Shea, P. H. Beton, A. Patanè
School of Physics and Astronomy
University of Nottingham
Nottingham NG7 2RD, UK
E-mail: amalia.patane@nottingham.ac.uk
S. Lara-Avila
Department of Microtechnology and Nanoscience
Chalmers University of Technology
Gothenburg 412 96, Sweden
S. Lara-Avila
National Physical Laboratory
Hampton Road, Teddington TW11 0LW, UK
J. Harknett, M. T. Greenaway
Department of Physics
Loughborough University
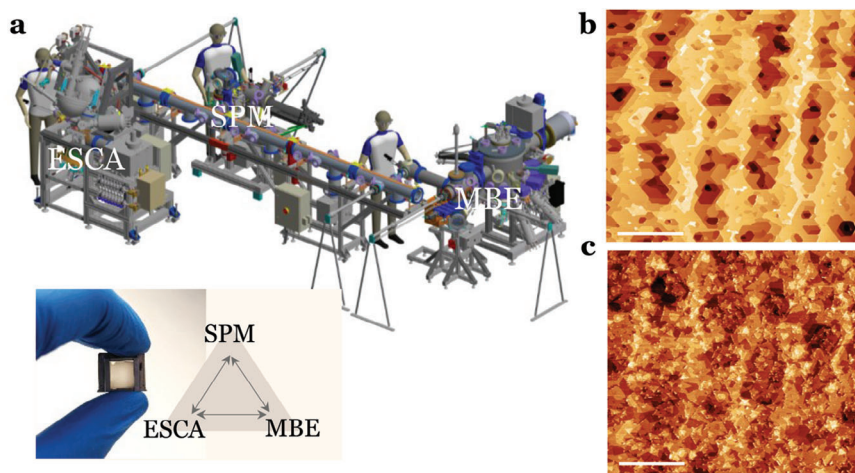Loughborough LE11 3TU, UK

1. Introduction

2D semiconductors (2SEM), constructed from materials that are a single or a few atoms thick, have the potential to overcome challenges in quantum science and modern electronics.[1] However, future advances require precise engineering of 2SEM and the development of high-quality heterostructures. A promising route toward this goal is provided by epitaxy of 2SEM on silicon carbide (SiC), which is graphitized to form homogenous large-area single-layer graphene, also referred to as epigraphene.[2] SiC-based technologies are well advanced and SiC substrates (conducting or semi-insulating) are commercially available,[3] providing a platform for a range of epigraphene-based technologies, ranging from resistance standards[4] and quantum electronics[5] to high-frequency applications.[6] Hybrid structures that combine graphene and 2SEM (2semgraphene) can expand these recent developments and overcome some of the limitations of graphene, such as the lack of a band gap and small optical absorbance.[7] In addition, 2semgraphene can provide a new, versatile building block in future applications.

To date, top–down approaches commonly used for the fabrication of 2SEM on graphene (e.g., exfoliation of van der Waals [vdW] crystals by "scotch-tape")[8] produce only small-area heterostructures with limited prospects for precise engineering of electronic properties at scale. Alternatively, bottom–up techniques based on epitaxy of 2SEM on different substrates are currently being developed.[9–14] This approach opens up opportunities for development of new materials and reduces the contamination of interfaces resulting from conventional approaches to exfoliation and, where relevant, exposure to chemical species in air. In this work, we report on a bespoke approach to epitaxy in ultra-high vacuum (UHV) and in situ microscopy and spectroscopy of 2semgraphene based on ultrathin layers of gallium selenide (GaSe).

Atomically-thin layers of GaSe possess an unconventional, electronic band structure with an inverted Mexican hat-shaped valence band (VB) and van Hove singularities in the density of

**ADVANCED
SCIENCE NEWS**

www.advancedsciencenews.com

NANO · MICRO

small

www.small-journal.com

Figure 1. a) Cluster (EPI2SEM) with three chambers in ultra-high vacuum (UHV) for growth by molecular beam epitaxy (MBE) and in situ analysis of the grown layers by electron spectroscopy for chemical analysis (ESCA) and scanning probe microscopy (SPM). Inset: optical image of GaSe on epigraphene and schematic of iterative growth and in situ analysis. Scanning tunneling microscopy images for b) epigraphene and c) GaSe (two to three layers) on epigraphene (scale bar = 500 nm).

states.[15–19] Their unique electronic properties, such as doping-induced tunable magnetism,[19] large mechanical flexibility, and sensitivity of the band structure to strain[20,21] are quite rare in semiconductors and they are paralleled by other interesting features, such as strong non-linear optical effects.[22,23] However, as for other 2SEM, experimental research on thin layers of GaSe can be hindered by defected interfaces or degradation in air. Thus, in many studies, the layers are bulk-like crystals;[22,24] alternatively, to prevent their oxidation, thin layers of GaSe are grown in UHV and capped by Se[16] or exfoliated in an inert atmosphere and capped by hBN.[25]

Here, we report on the electronic properties of scalable GaSe/graphene interfaces and their use in ultrathin optical sensors. The GaSe/graphene heterostructures are grown by molecular beam epitaxy (MBE) and studied in situ by electron diffraction, scanning probe microscopy (SPM), and electron spectroscopy for chemical analysis (ESCA) within a bespoke UHV cluster. We show that the hexagonal crystal lattice of GaSe aligns in the layer plane with that of graphene. The 2semgraphene heterostructure features a centrosymmetric (D_{3d}) polymorph of GaSe, a charge dipole at the GaSe/graphene interface, and an electronic band structure that is tunable by the GaSe layer thickness. All these features are scalable, as demonstrated experimentally and modeled by density functional theory (DFT). The 2semgraphene is used in ultrathin optical sensors that exploit the photoactive GaSe and the sensitivity of its interface with the graphene channel to photogenerated carriers. This proof of concept for photon sensing at a heterointerface has the potential for the further implementation of 2semgraphene as a functional building block in device architectures and integrated applications.

2. Results and Discussion
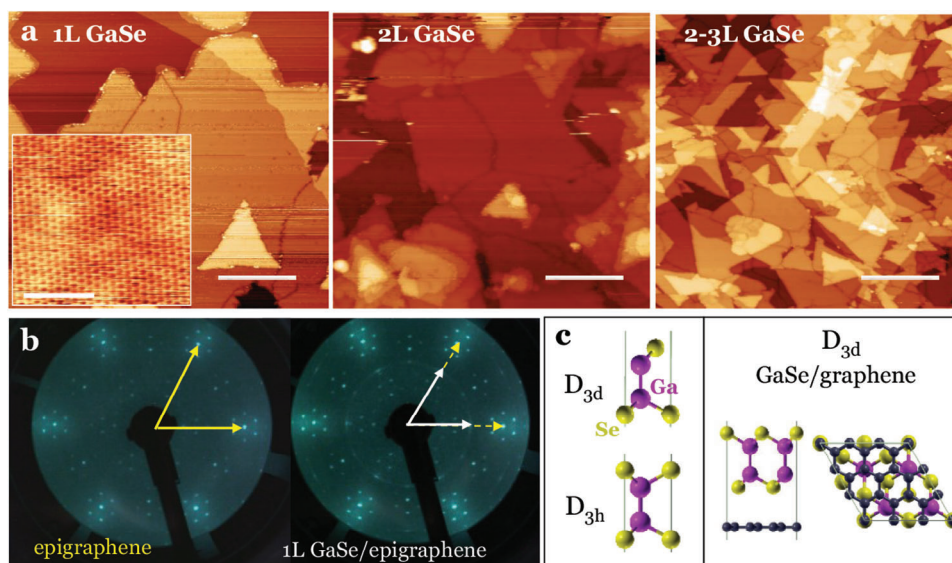
2.1. Epitaxy of GaSe Coupled to Graphene

Figure 1a shows the UHV cluster (EPI2SEM) with three chambers for EPItaxial growth of 2SEM by MBE and in situ analysis by

SPM and ESCA. Within EPI2SEM, samples could be transferred between the three chambers for single or multiple iterations of growth and analysis in UHV. Thin layers of GaSe were grown by MBE on epigraphene substrates (area of up to 10×10 mm^2) that were either produced in situ in the SPM chamber or ex situ (Figure 1a and Experimental Section). The growth of the GaSe layers with a range of nominal thicknesses, l, from 1 vdW layer (1L = 0.83 nm) to 11L was monitored by reflection high energy electron diffraction (RHEED). We estimated the layer thickness from the growth rate and calibration studies by scanning tunneling microscopy (STM) of thin layers ($l \leq 3L$).

Figures 1b and 2a show STM images for epigraphene (Figure 1b) and thin layers of GaSe ($l \leq 3L$) (Figures 1c and 2a). The initial stages of the GaSe growth on epigraphene progress via the formation of triangular crystalline islands with lateral size in the range 100–500 nm and thickness of 0.8 nm. The nucleation of the islands occurs both at step edges and along the extended flat terraces of graphene on SiC. Following the growth of thicker layers ($l > 3L$), the GaSe islands tend to nucleate more randomly and, in some instances, form concentric stacks characteristic of a spiral-island growth mode (Figure S1, Supporting Information).

The long-range ordering of the layers is probed by low-energy (100 eV) electron diffraction (LEED) in the SPM chamber. The spots in the LEED patterns for epigraphene and 1L GaSe (Figure 2b) show that the crystal lattice of GaSe tends to align in the layer plane with that of the underlying graphene. This in-plane alignment is also observed in 2L and 3L GaSe, but is not detected in thicker ($l > 3L$) samples (Figure S2, Supporting Information) due to the small penetration depth of the electron beam and orientational disorder in the higher layers, which have grains with smaller lateral dimensions.

From the analysis of the high-resolution STM images and LEED patterns, we estimate the in-plane lattice constants a_g = (2.4 ± 0.1) Å and a_{GaSe} = (3.9 ± 0.2) Å for graphene and 1L GaSe, respectively, corresponding to a lattice mismatch of $(a_{GaSe} - a_g)/a_g \approx 62\%$. The value of a_{GaSe} is in agreement with the values for the hexagonal lattice of centrosymmetric

**ADVANCED
SCIENCE NEWS**
www.advancedsciencenews.com

NANO · MICRO
small
www.small-journal.com

Figure 2. a) Scanning tunneling microscopy (STM) images for 1 layer (L), 2L, and 2–3L GaSe on epigraphene (scale bar = 200 nm). The inset (left) shows a high-resolution STM image for 1L GaSe (scale bar = 4 nm). b) Low energy electron diffraction (LEED) image for epigraphene (left) and for 1L GaSe on epigraphene (right). Arrows mark the diffraction spots for graphene (yellow, left and right) and 1L GaSe (white, right). Each of the spots for graphene is surrounded by six satellite spots associated with the $(6\sqrt{3} \times 6\sqrt{3})R30°$ buffer layer of SiC. c) Left: polymorphs of GaSe with axial-symmetry (D_{3h}) and centro-symmetry (D_{3d}). Right: In-plane and side views of D_{3d} GaSe on graphene, as modeled by density functional theory.

(D_{3d}, $a_{GaSe} = 3.809$ Å) and non-centrosymmetric (D_{3h}, $a_{GaSe} = 3.797$ Å) isolated GaSe, as modeled by DFT (Figure 2c and Experimental Section). Studies of epitaxial GaSe on sapphire[26,27] and Si[27] substrates have identified distinct atomic configurations for GaSe, corresponding to those predicted for D_{3d} and D_{3h} GaSe.[28] The D_{3h} polymorph of GaSe features a Se–Ga–Ga–Se tetralayer (TL) with mirror symmetry: each Ga atom is covalently bonded to three equidistant Se atoms and another Ga atom; in contrast, for the D_{3d} polymorph, the Ga–Se bonds in the upper and lower part of the centrosymmetric TL have a rotational mismatch of 60°.
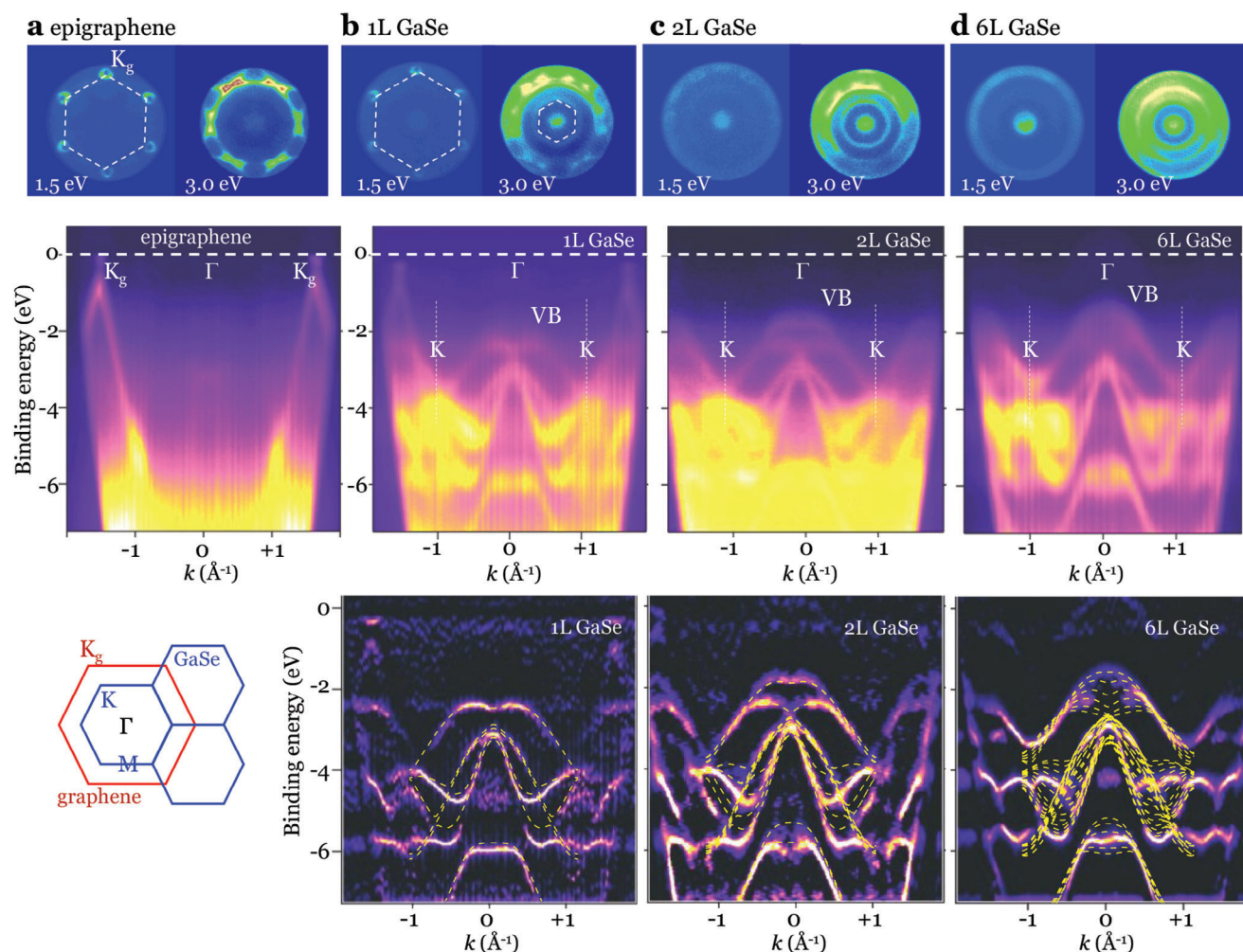
The interfaces formed by the two polymorphs with graphene have similar formation energies. For the modeling, we examined a heterostructure with aligned graphene and GaSe lattices. We considered two configurations with distinct relative lateral displacements of the two lattices and neglected the effects of large-scale (moiré) lattice reconstruction. The two structures correspond to heterostructures where one of the graphene or GaSe atoms is in the center of one of the hexagonal unit cells. For each configuration, we calculated an equilibrium interlayer distance at the GaSe/graphene interface of $d = 0.35$ nm (Figure 2c; Figure S3, Supporting Information) and a similar band structure.

2.2. In Situ Band Engineering of GaSe/Graphene Heterostructures

The alignment of 1L GaSe with graphene measured by LEED (Figure 2b) is confirmed by angle-resolved photoemission spectroscopy (ARPES). **Figure 3** shows the room temperature (T = 300K) ARPES data for epigraphene (Figure 3a) and 1L GaSe/epigraphene (Figure 3b). The in-plane hexagonal Brillouin zones (BZ) for epigraphene and GaSe are overlaid on the ARPES

constant energy surface plots of Figure 3a,b, showing the high-symmetry points (K and M) in the BZ of graphene and of 1L GaSe. The constant energy ARPES slices of Figure 3a show the six Dirac cones for the n-doped graphene on SiC. From the energy band dispersions along the high-symmetry K-directions in the BZ, we estimate a Fermi energy $E_F = 0.43 \pm 0.05$ eV above the neutrality point of graphene, corresponding to an electron density $n = (E_F/\hbar v_F)^2/\pi = 1.4 \times 10^{13}$ cm^{-2}, where $v_F = 10^6$ ms^{-1} is the electron Fermi velocity in graphene.[29] Such a high electron concentration is typical for epigraphene due to donor states associated with C- and Si-dangling bonds in the SiC buffer layer.[30] Following the growth of 1L GaSe on epigraphene, the Dirac cones and energy dispersion of graphene are well preserved overall, but additional bands emerge in the ARPES data (Figure 3b). The ARPES constant energy surface plots show that the BZs of graphene and 1L GaSe are well-aligned, indicating a preferential alignment of 1L GaSe with the underlying graphene lattice.

The ARPES plots of the photoelectron intensity and of its second derivative as a function of energy and k-momentum along the Γ-K-directions show that the valence band of GaSe evolves from an inverted Mexican hat-shaped band in 1L (Figure 3b) and 2L GaSe (Figure 3c) to a parabolic band in 6L GaSe (Figure 3d). With decreasing l, the valence band maximum (VBM) shifts away from Γ toward the K-points with binding energy of $E = 1.4$, 1.8, and 2.2 eV in the 6L, 2L, and 1L GaSe, respectively. The same band structure was observed at different positions over large (>10^2 μm^2) areas, demonstrating the tunability and scalability of the electronic properties of 2semgraphene. In particular, electron–phonon interactions at room temperature do not prevent the observation of an inverted Mexican hat-shaped VB in thin GaSe layers, which have a depth of up to ≈100 meV in 1L GaSe.

**ADVANCED
SCIENCE NEWS**

www.advancedsciencenews.com
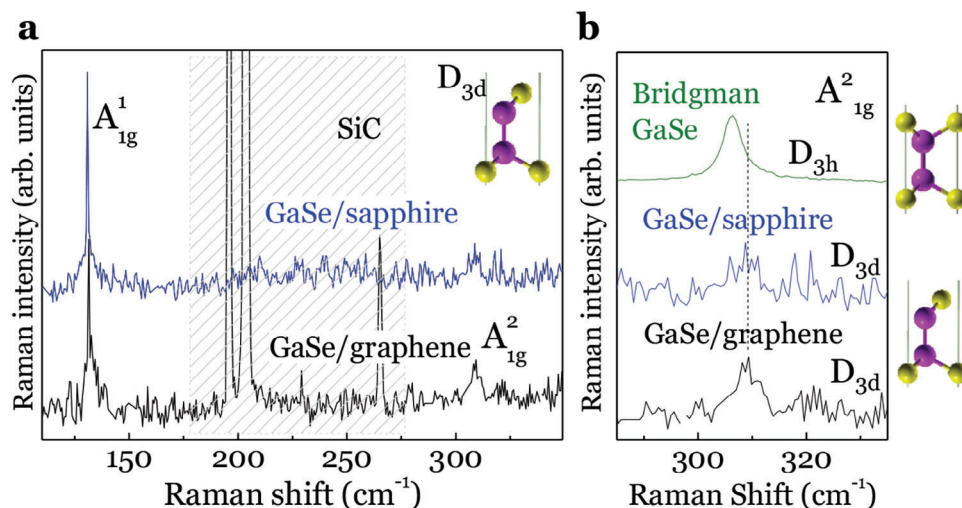
NANO · MICRO

small

www.small-journal.com

Figure 3. Constant energy ARPES slices acquired at a binding energy of 1.5 and 3.0 eV for a) epigraphene, b) 1L, c) 2L, and d) 6L GaSe on epigraphene. The hexagonal Brillouin zones (BZ) for graphene and GaSe are overlaid on the ARPES slices in parts (a,b). The bottom panel in part (a) shows the momentum alignment of the BZ of graphene (red) and GaSe (blue). Each middle panel (a–d) shows the ARPES data along high-symmetry directions. Energies are relative to the Fermi level (dashed horizontal line). The bottom panels (b–d) show the second derivative of the photoelectron intensity versus energy and k-momentum. Dashed yellow lines are the calculated bands for D_{3d} GaSe.

The GaSe/graphene heterostructure features a dominant D_{3d} polymorph of GaSe, as probed by Raman spectroscopy (**Figure 4a**). The room temperature Raman spectra for 6L GaSe on epigraphene show the A^1_{1g} and A^2_{1g} modes at 131.5 and 308.0 cm^{-1}, respectively. The A^2_{1g} mode is blue-shifted by 2 cm^{-1} relative to the same mode for the D_{3h} polymorph of Bridgman-grown GaSe (Figure 4b) and its position is aligned with that of the A^2_{1g} mode in centrosymmetric (D_{3d}) GaSe on sapphire.[26] The Raman modes are weaker in thinner layers (Figure S5, Supporting Information) and the position of the Raman modes does not change in GaSe flakes that are exfoliated from as-grown GaSe/epigraphene and transferred from the epigraphene onto a mica-substrate (Figure S6, Supporting Information). Thus, we exclude any effect of the graphene substrate on the observed Raman shifts of GaSe grown on epigraphene.

A comparison of the calculated band structure for D_{3d} GaSe on graphene (**Figure 5a**) and D_{3d} GaSe (Figure 5b) shows that the energy bands of GaSe are overall well preserved in the

heterostructure with a weak hybridization of electronic states at the GaSe/graphene interface. We note that the K-point of graphene (K_g) is close to the M-point of the extended BZ of GaSe (see Brillouin zones in the inset of Figure 5a), leading to a stronger hybridization of states around these points. This hybridization is sensitive to the polymorph of GaSe, as shown in Figure 5c for D_{3h} GaSe on graphene. We also note that the calculated band gap energies for 1L GaSe with ($E_{g\text{-GaSe}}$) and without (E_{GaSe}) the graphene layer are very similar with a difference ($E_{g\text{-GaSe}} - E_{GaSe} = 14$ meV) that tends to decrease in thicker GaSe layers.

The calculated band structure reproduces many features revealed by the ARPES data (Figure 3b–d), including the weak hybridization of the graphene and GaSe states and the evolution of the valence band with increasing layer thickness (see also Figure S7, Supporting Information). In particular, DFT describes well the form of the VB at the VBM and the VB minimum at Γ. From the energy dispersions along the Γ-K direction for 1L (2L) GaSe,

**ADVANCED
SCIENCE NEWS**

www.advancedsciencenews.com

NANO · MICRO

small

www.small-journal.com

Figure 4. a) Room temperature Raman spectra of GaSe layers on epigraphene (black) and sapphire (blue) substrates, showing two dominant A_{1g}^1 and A_{1g}^2 modes. The shaded regions indicate the spectral range containing peaks for the SiC substrate. The inset shows the D_{3d} polymorph of GaSe. b) Comparison of the A_{1g}^2 peak in GaSe grown by MBE on epigraphene and sapphire (D_{3d}) and Bridgman-grown (D_{3h}) GaSe ($\lambda = 633$ nm, $P = 0.09$ mW).
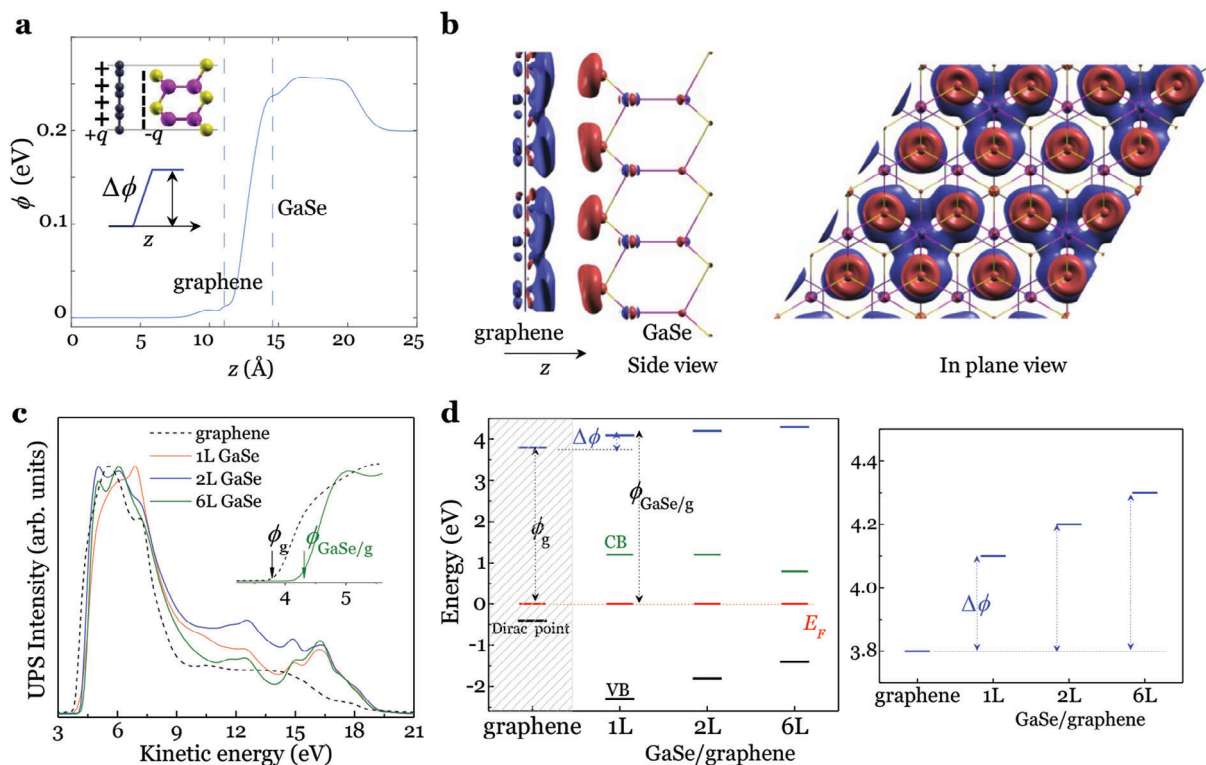
we obtain a hole effective mass $m_h^* = 1.5$ m_e $(1.1m_e)$ at the VBM and $m_h^* = -0.8$ m_e $(-0.8$ $m_e)$ at Γ, where m_e is the electron mass in vacuum.

The binding mechanism between the GaSe and graphene layers is a combination of effects, including the dispersive (London) forces and the electrostatic binding due to charge transfer. At equilibrium, the GaSe/graphene interface features a redistribution of charge with an accumulation of negative charge at the interface region next to the GaSe and a charge depletion close to graphene. The computed charge density at both interfaces creates a potential that varies along the z-direction, perpendicular to the layer plane, and an energy potential step of up to $\Delta\phi$ =

0.25 eV at the GaSe/graphene interface (**Figure 6**a,b; Figure S4, Supporting Information). The calculated value of $\Delta\phi$ is in agreement with that derived from the difference of the work functions of 1L GaSe/graphene ($\phi_{GaSe/g}$) and epigraphene (ϕ_g), as measured by ultraviolet photoemission spectroscopy (UPS) in the ESCA chamber. From the secondary electron low-energy cutoff of the UPS spectra, we obtain $\phi_g = 3.8$ eV and $\phi_{GaSe/g} = 4.1$ eV, corresponding to $\Delta\phi = \phi_{GaSe/g} - \phi_g = 0.3$ eV. With increasing layer thickness, the values of $\phi_{GaSe/g}$ and $\Delta\phi$ increase: $\phi_{GaSe/g} = 4.2$ eV ($\Delta\phi = 0.4$ eV) and 4.3 eV ($\Delta\phi = 0.5$ eV) in 2L and 6L GaSe, respectively (Figure 6c). The results of the UPS and ARPES experiments are summarized in the energy band diagram of Figure 6d,
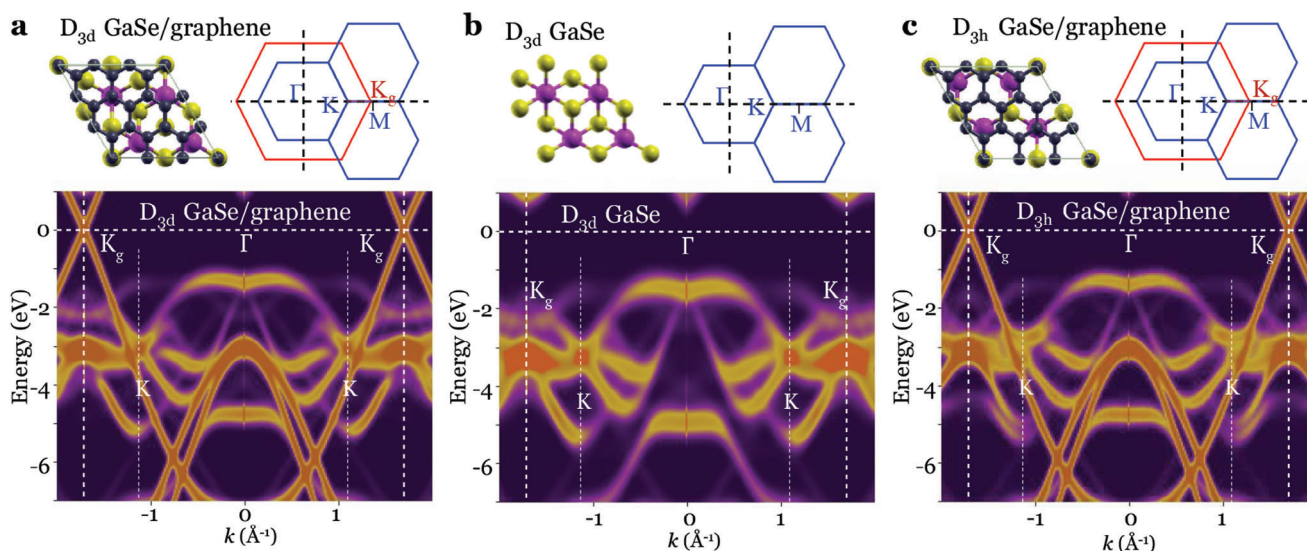
Figure 5. Spectral density plots showing the unfolded band structure of a) 1 layer (L) D_{3d} GaSe on graphene, b) 1L D_{3d} GaSe, and c) 1L D_{3h} GaSe on graphene. The color map corresponds to the spectral weight in the unfolded Brillouin zone (BZ). Horizontal dashed line shows the Fermi energy. Vertical lines show the high symmetry points in the BZ of graphene (K_g) and GaSe (K). The insets above mains panels show the in-plane view of the GaSe/graphene crystal structure and the momentum alignment of the high symmetry points in the graphene (red) and GaSe (blue) BZ.

ADVANCED
SCIENCE NEWS

www.advancedsciencenews.com

NANO · MICRO

small

www.small-journal.com

Figure 6. a) Calculated potential energy ϕ profile along the z-direction (perpendicular to the layer plane) due to the charge dipole (inset) at the GaSe/graphene interface. Inset: energy potential step $\Delta\phi$ at the GaSe/graphene interface. b) Isosurfaces of Δn, the difference in the number density of electrons between the graphene/GaSe heterostructure and the individual GaSe and graphene layers. The isovalue is 0.0001 (e/a_o^3), where a_o is the Bohr radius. Red (blue) surfaces correspond to positive (negative) values of Δn. c) Ultraviolet photoemission spectroscopy (UPS) data for epigraphene and 1 layer (L), 2L, and 6L GaSe/epigraphene. Inset: UPS data over a narrow energy range. The work functions of graphene (ϕ_g) and GaSe/graphene ($\phi_{GaSe/g}$) are derived by extrapolating the rising edge of the UPS signal down to zero. d) Fermi energy, E_F (red) and valence band maximum edge (VB) (black), as derived from ARPES and UPS data. The blue lines correspond to the vacuum level. The conduction band (CB) edge (green) is estimated from the band gap energy, as measured in ref.[16] and from the VB edge measured in this work. Right inset: work function for graphene (ϕ_g) and GaSe/graphene ($\phi_{GaSe/g}$) as measured by UPS. The difference, $\phi_{GaSe/g} - \phi_g$ corresponds to the potential step $\Delta\phi$ at the GaSe/graphene interface.

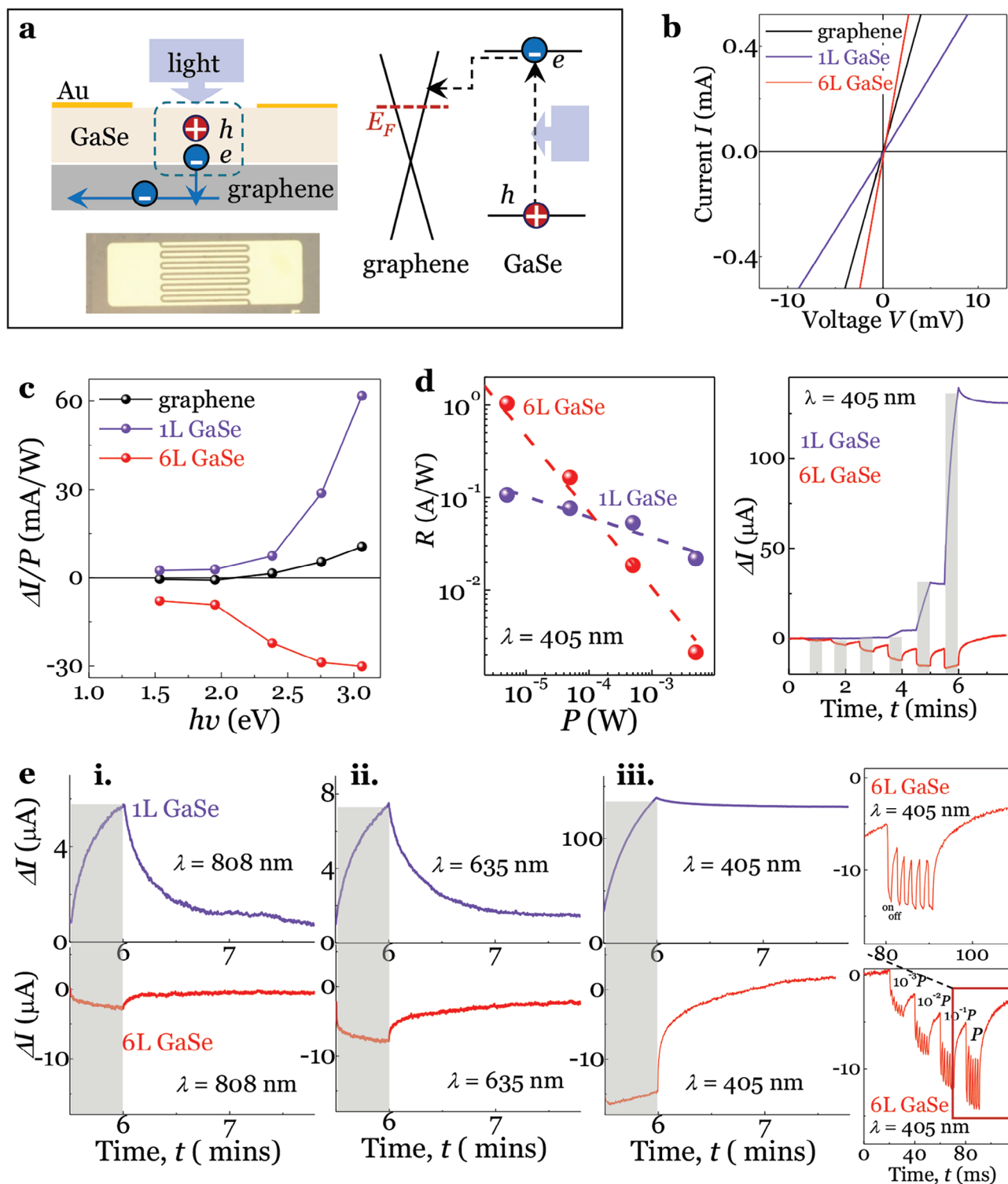showing the Fermi level (E_F), band edges, ϕ and $\Delta\phi$ for all samples.

Our data and those in the literature[16,31] indicate that GaSe layers on graphene are n-type semiconductors. The n-type conductivity of GaSe contrasts with the intrinsic p-type behavior predicted for GaSe:[32] 1L GaSe is weakly p-type due to intrinsic defects; also, its p-type doping cannot be compensated. Thus, we conclude that in the GaSe/graphene heterostructure, the n-type graphene leads to an effective modulation doping of GaSe via transfer of electrons from the graphene onto GaSe. However, we do not exclude charge transfer due to defects that can lead to the accumulation of negative surface charges in the GaSe layer, thus accounting for the increase of $\Delta\phi$ with increasing l.

2.3. Ultra-Thin Optical Sensors

Here, we examine further the GaSe/graphene interface and its potential for optical sensing. The GaSe layer is well known to be a photoactive medium with a large optical absorption coefficient ($>10^6$ cm^{-1} in the UV[26]). Thus, the large built-in potential at the GaSe/graphene interface (Figure 6a) offers a platform for separation of the photocreated carriers and transfer of pho-

toelectrons into the graphene transport channel. To assess this proof of concept, we consider the device structure of **Figure 7**a and its electrical properties in the dark (Figure 7b) and under light (Figure 7c–e). Our planar devices are based on the 2sem-graphene heterostructures described in previous sections. Interdigitated Au-electrodes are fabricated by evaporation of Au onto the GaSe surface through a shadow mask (Figure 7a and Experimental Section), and the electrical measurements are conducted in vacuum to avoid contamination of the layers in air or their degradation under light.

As illustrated in Figure 7b, in the dark, the current–voltage (I–V) curves for devices based on epigraphene and GaSe/epigraphene exhibit a similar ohmic-like conductivity. Under light excitation, a photocurrent $|\Delta I|$ is measured in all devices even at low applied biases (<10 mV), with a larger responsivity $R = |\Delta I|/P$ observed in devices based on GaSe (Figure 7c). Interestingly, the behavior of 1L and 6L GaSe layers is qualitatively different: the positive photocurrent in 1L GaSe has opposite sign to the negative photocurrent in 6L GaSe (Figure 7c); the responsivity R has a weaker dependence in 1L GaSe (Figure 7d); also, the rise and recovery times of the photocurrent are longer in thin layers. Figure 7e shows the temporal dependence of ΔI for 1L and 6L GaSe under excitation by photons with different wavelengths.

ADVANCED
SCIENCE NEWS

www.advancedsciencenews.com

NANO · MICRO

small

www.small-journal.com

Figure 7. a) Schematic and optical image of a representative device and of the photon sensing mechanism. b) Current–voltage curves in the dark for epigraphene, 1 layer (L) GaSe, and 6L GaSe on epigraphene. c) Dependence of $\Delta I/P$ on photon energy $h\nu$ for epigraphene, 1L GaSe, and 6L GaSe on epigraphene ($T = 300$K, $V = +10$ mV, $P = 0.5$ mW). Here, ΔI is the photocurrent and P is the laser power. d) Left: Absolute value of the responsivity R versus P for 1L and 6L GaSe at $\lambda = 405$ nm. Lines are fit to the data by P^{-a}, where $a = 0.2$ and 0.9 for 1L and 6L, respectively. Right: Multiple cycles of light on (shaded regions) and off at $\lambda = 405$ nm and increasing laser powers. e) Photocurrent versus time under photoexcitation of 1L and 6L GaSe with laser of wavelength e-i) $\lambda = 808$ nm, e-ii) 635 nm, and e-iii) 405 nm ($T = 300$ K, $V = +10$ mV, and $P = 5$ mW). The light is switched on (shaded rectangle) and then off. The inset in part (iii) shows repeated cycles of light on/off at a given power $P = 5$ mW (top) and at increasing P (bottom) for 6L GaSe ($\lambda = 405$ nm). At each power, the light is switched on and off several times.

When the 1L GaSe device is driven out of equilibrium by light, the current does not return to the initial unperturbed dark state and the positive persistent photocurrent (PPP) lasts for several hours. The PPP is observed in 1L and 2L GaSe (not shown), but not in 6L GaSe; also, it is observed under multiple cycles of light on/off (Figure 7d).

We first consider the positive photocurrent and PPP in 1L GaSe. The charge dipole and built-in potential at the GaSe/graphene interface act to separate the photogenerated electron–hole pairs, leading to a preferential transfer of photocreated electrons in the graphene layer (Figure 7a). The indirect nature of the band gap of 1L GaSe can delay band-to-band recombination, leading to an accumulation of positive charge in GaSe. The heavy (localized) holes in the valence band can undergo a very slow quenching after light illumination, thus acting as a gate for graphene and causing a persistent photoconductive gain.

As the layer thickness increases to 6L, the charge transfer at the GaSe/graphene interface changes. This is reflected in the sign of the photocurrent ΔI as well as in the dependence of the responsivity R on P. A fit to the R–P curve by a power law ($R \propto P^{-a}$) gives a coefficient $a = 0.2$ and $a = 0.9$ in 1L and 6L GaSe, respectively (Figure 7d). This corresponds to a dependence of $|\Delta I|$ on P given by $|\Delta I| = PR \propto P^b$, with $b = 1-a = 0.8$ and $b = 0.1$ in 1L and 6L GaSe, respectively. The weaker dependence of ΔI on P in 6L GaSe is suggestive of an increasing carrier recombination rate with increasing P. This is expected in thicker layers due to the direct nature of the band gap and an effective smaller interfacial electric field experienced by the photocreated carriers, leading to a less efficient charge transfer at the interface with graphene. This can also account for a shorter lifetime of the photocreated holes, and hence, for the faster temporal response of the measured photocurrent in 6L GaSe (Figure 7e). We also note that transport of photocreated carriers can occur in different regions of the GaSe/graphene heterostructure: the GaSe layer and the GaSe/graphene interface. To examine the contribution to the photoresponse from the GaSe layer, we have compared the photocurrent of 6L GaSe grown on sapphire with that of 6L GaSe on graphene. For 6L GaSe on sapphire, the photocurrent is much smaller (Figure S8, Supporting Information). Thus, we conclude that the photoconductivity in our samples is dominated by charge transport at the GaSe/graphene interface.

For all samples, the energy band alignment and the Raman studies are consistent with an increased electron density in the graphene layer under light than in the dark (Figure S9, Supporting Information). Thus, the negative photoconductivity in thicker GaSe layers suggests that despite the increase of electron density in the graphene channel under light, the conductivity of graphene is reduced due to an increased electron scattering rate. This is further supported by the decrease of responsivity with increasing P (Figure 7d), which we assign to an increased scattering effect between phonons and charge carriers under an increasing carrier generate rate, a phenomenon recently reported in Si/graphene junctions.[33] Finally, the photocurrent under optical excitation with laser energy below the band gap of GaSe is assigned to the photo-activation of deep levels in the GaSe. As shown in Figure 7c, the photocurrent signal at these energies is much smaller than at energies above the band gap (>2 eV). In addition, a small contribution to the photocurrent of all samples can arise from the photo-activation

of deep levels in the SiC substrate.[34,35] Deep levels can act to photodope the graphene channel, causing a PPP due to their slow (hours) charging/discharging.[36] This phenomenon is expected to be more prominent in thinner layers due to the discontinuous coverage of the GaSe layer (Figure 2).

3. Conclusion

In summary, we use molecular beam epitaxy and in situ microscopy and electron spectroscopy techniques in UHV to grow and study ultrathin layers of GaSe on epigraphene. The epitaxial growth progresses via the formation of crystalline GaSe islands both at step edges and along the extended flat terraces of graphene. The first GaSe layers tend to align in the layer plane with the underlying lattice of graphene and exhibit an electronic band structure and energy band alignment with graphene that are tunable by the GaSe layer thickness, as measured by ESCA and predicted by DFT for the centrosymmetric polymorph (D_{3d}) of GaSe. The properties reported here are scalable, and the GaSe/graphene interface provides an effective platform for photon sensing. In the proof of concept GaSe-based device described in this work, the GaSe/graphene interface is sensitive to charges photogenerated in the photoactive GaSe layer. For all samples, the electron density in the graphene layer increases under light. However, a positive or negative photocurrent is measured in devices based on thin and thick GaSe/graphene heterostructures, respectively. The light-induced electron transfer at the GaSe/graphene interface can be utilized to promote long-lived heavy holes in the inverted Mexican-hat valence band of GaSe for investigations of carrier correlation phenomena, which require controlled and tunable hole doping.[15–19] In particular, the positive photocurrent and optical memory in single layer GaSe on graphene offer prospects for surface charge sensing, including optical imaging circuits and memories.[37] Finally, transfer of the grown GaSe layers from epigraphene onto a different substrate, such as the preliminar transfer of thin layers of GaSe onto flexible mica, has the potential for further advances and developments of scalable materials and devices on different platforms.

4. Experimental Section

Epitaxy and Substrates: The MBE system (PRO-75, Scienta Omicron) is capable of growth on rotating substrates with diameters of up to 3 in. Epigraphene substrates were produced at Graphensic or within EPI2SEM. Epigraphene from Graphensic was produced by thermal decomposition of a 4-in. diameter 4H-SiC (0001) semi-insulating wafer at temperatures above 1800 °C in argon atmosphere (pressure of 1 bar), which was subsequently diced into 10 × 10 mm² pieces. The substrates produced in EPI2SEM were obtained by repeatedly flash annealing heavily doped SiC (PAM-XIAMEN) at 1400 °C in ultrahigh vacuum (UHV) (base pressure <2 × 10⁻¹⁰ mbar), as outlined in ref.[38]. In the MBE growth of GaSe, both types of epigraphene substrates were initially annealed in the MBE chamber at 800 °C for 40 min to remove potential surface contamination. The substrate temperature was then reduced to 550 °C for the growth of GaSe. High-purity elemental Ga (7N) and Se (6N+) were evaporated from PEZ 63 production effusion and VSCS valved Se cracker cells, respectively, both from Dr. Eberl MBE-Komponenten. The Ga beam flux was measured by ion gauge and controlled by the temperature of the cell; while the Se flux was controlled by both the opening of the source valve and Se reservoir temperature. The growth of GaSe (growth rate of ≈ 1.7 nm min⁻¹) was monitored by reflection high-energy electron diffraction (RHEED).

SPM: In situ surface analysis was conducted by STM in UHV at room temperature using a VT-AFM/XA system from ScientaOmicron with in-house electrochemically etched W tips. GaSe layers with thicknesses above 2L were studied ex situ by AFM using an Asylum Research Cypher-S AFM system under ambient conditions. The system was operated in tapping mode using amplitude modulation. All SPM data was processed using the Gwyddion software package.[39]

ESCA: ARPES and UPS measurements were conducted using a Scienta Omicron nanoESCA equipped with a Focus HIS 14 HD UV photon source with energy $h\nu = 21.219$ eV. The ESCA was operated in energy filtered mode with a pass energy of 25 eV and slit width of 0.5 mm, leading to an energy resolution of 50 meV. For ARPES, photoelectrons were collected from a region of $\approx 100 \times 100$ μm^2. The experiments were conducted for several areas of the sample (each 10×10 mm^2) to probe its uniformity. Both ARPES and UPS were conducted with the photoemission electron microscopy (PEEM) optics in telescopic mode with an extractor voltage of 12 kV. The Fermi energy, energy resolution, and k calibration were confirmed through measurements on a gold reference sample.

Optical Studies: Raman spectroscopy studies were performed ex situ in air using a micro-Raman setup comprising a He-Ne laser (632.8 nm) or a frequency doubled Nd:YVO4 laser ($\lambda = 532$ nm), an x–y–z motorized stage, and an optical confocal microscope system from Horiba Scientific (0.5 m-long monochromator; 1200 groves mm^{-1} grating). The signal was detected by a Si charge-coupled device camera. The laser beam diameter was focused to ≈ 1 μm using a 100× objective. Low powers (<2.3 mW) were used to minimize heating and oxidation effects.

Device Fabrication and Transport: For the deposition of interdigitated Au-electrodes, a rigid metal-based shadow mask was placed in close contact with the GaSe surface and no polymers or solvents were used; thus, avoiding any contamination of the layers. The evaporated contacts had an approximate thickness of 100 nm. The resulting devices had a channel width of ≈ 18 mm and a channel length of 50 μm. Electrical measurements were acquired using a Keithley 2400 SourceMeter. Unfocused laser light with wavelengths between $\lambda = 1080$ nm and 405 nm was provided by a fiber-coupled system manufactured by Changchun New Industries Optoelectronics Technology Co., Ltd. The power densities were estimated using a Thorlabs PM100D power meter. All transport measurements were conducted in vacuum (pressure $\approx 10^{-6}$ mbar).

Density Functional Theory: First-principles calculations were carried out within the framework of DFT by using the plane-wave pseudopotential approach as implemented in the Quantum Espresso code.[40,41] The generalized gradient approximation formulated by Perdew, Burke, and Ernzerhof was used as the exchange-correlation functional.[42] To calculate the band structure of the mono- and multi-layer structures, vacuum spaces with a thickness greater than the layer thicknesses were used which, along with the Coulomb potential truncation scheme of ref.[43], separated the layers from their periodic images. The self-consistent calculations were solved on at least a $18 \times 18 \times 6$ Monkhurst Pack grid of k-points with plane-wave energy cut-offs set at 80 Ry.[44] To take into account the effect of non-local van der Waals forces, the Grimme-D3 vdW correction scheme[45] (a comparison of structural relaxation with the vdW correction Grimme-D3M [Becke–Johnson damping][46] is shown in the Supporting Information) was implemented. The GaSe structures were relaxed so that the residual inter-atomic forces were less than 10^{-4} Ry Bohr^{-1}. The unfolding of the band structure for the heterostructures was performed using the BandUP(py) code.[47,48]

Supporting Information

Supporting Information is available from the Wiley Online Library or from the author.

Conflict of Interest

The authors declare no conflict of interest.

Data Availability Statement

The data that support the findings of this study are available from the corresponding author upon reasonable request.

[1] W. Cao, H. Bu, M. Vinet, M. Cao, S. Takagi, S. Hwang, T. Ghani, K. Banerjee, *Nature* **2023**, *620*, 501.

[2] C. Berger, Z. Song, X. Li, X. Wu, N. Brown, C. Naud, D. Mayou, T. Li, J. Hass, A. N. Marchenkov, E. H. Conrad, P. N. First, W. A. de Heer, *Science* **2006**, *312*, 1191.

[3] C. R. Eddy, D. K. Gaskill, *Science* **2009**, *324*, 1398.

[4] A. Tzalenchuk, S. Lara-Avila, A. Kalaboukhov, S. Paolillo, M. Syväjärvi, R. Yakimova, O. Kazakova, T. J. B. M. Janssen, V. Fal'ko, S. Kubatkin, *Nat. Nanotechnol.* **2010**, *5*, 186.

[5] V. S. Prudkovskiy, Y. Hu, K. Zhang, Y. Hu, P. Ji, G. Nunn, J. Zhao, C. Shi, A. Tejeda, D. Wander, A. De Cecco, C. B. Winkelmann, Y. Jiang, T. Zhao, K. Wakabayashi, Z. Jiang, L. Ma, C. Berger, W. A. de Heer, *Nat. Commun.* **2022**, *13*, 7814.

[6] Y.-M. Lin, C. Dimitrakopoulos, K. A. Jenkins, D. B. Farmer, H.-Y. Chiu, A. Grill, P. h. Avouris, *Science* **2010**, *327*, 662.

[7] R. R. Nair, P. Blake, A. N. Grigorenko, K. S. Novoselov, T. J. Booth, T. Stauber, N. M. R. Peres, A. K. Geim, *Science* **2008**, *320*, 1308.

[8] P. Solís-Fernández, M. Bissett, H. Ago, *Chem. Soc. Rev.* **2017**, *46*, 4572.

[9] Y. Kim, S. S. Cruz, K. Lee, B. O. Alawode, C. Choi, Y. Song, J. M. Johnson, C. Heidelberger, W. Kong, S. Choi, K. Qiao, I. Almansouri, E. A. Fitzgerald, J. Kong, A. M. Kolpak, J. Hwang, J. Kim, *Nature* **2017**, *544*, 340.

[10] L. Wang, X. Xu, L. Zhang, R. Qiao, M. Wu, Z. Wang, S. Zhang, J. Liang, Z. Zhang, Z. Zhang, W. Chen, X. Xie, J. Zong, Y. Shan, Y. Guo, M. Willinger, H. Wu, Q. Li, W. Wang, P. Gao, S. Wu, Y. Zhang, Y. Jiang, D. Yu, E. Wang, X. Bai, Z.-J. Wang, F. Ding, K. Liu, *Nature* **2019**, *570*, 91.

[11] X. Xu, T. Guo, H. Kim, M. K. Hota, R. S. Alsaadi, M. Lanza, X. Zhang, H. N. Alshareef, *Adv. Mater.* **2022**, *34*, 2108258.

[12] L. Shi, *Nat. Nanotechnol.* **2024**, *19*, 145.

[13] S. Forti, A. Rossi, H. Büch, T. Cavallucci, F. Bisio, A. Sala, T. O. Menteş, A. Locatelli, M. Magnozzi, M. Canepa, K. Müller, S. Link, U. Starke, V. Tozzini, C. Coletti, *Nanoscale* **2017**, *9*, 16412.

[14] A. Rossi, H. Büch, C. Di Rienzo, V. Miseikis, D. Convertino, A. Al-Temimy, V. Voliani, M. Gemmi, V. Piazza, C. Coletti, *2D Mater.* **2016**, *3*, 031013.

[15] D. V. Rybkovskiy, A. V. Osadchy, E. D. Obraztsova, *Phys. Rev. B* **2014**, *90*, 235302.

**ADVANCED
SCIENCE NEWS**

www.advancedsciencenews.com

**NANO · MICRO
small**

www.small-journal.com

[16] Z. Ben Aziza, D. Pierucci, H. Henck, M. G. Silly, C. David, M. Yoon, F. Sirotti, K. Xiao, M. Eddrief, J.-C. Girard, A. Ouerghi, *Phys. Rev. B* **2017**, *96*, 035407.

[17] Z. Ben Aziza, V. Zólyomi, H. Henck, D. Pierucci, M. G. Silly, J. Avila, S. J. Magorrian, J. Chaste, C. Chen, M. Yoon, K. Xiao, F. Sirotti, M. C. Asensio, E. Lhuillier, M. Eddrief, V. I. Fal'ko, A. Ouerghi, *Phys. Rev. B* **2018**, *98*, 115405.

[18] M.-W. Chen, H. Kim, D. Ovchinnikov, A. Kuc, T. Heine, O. Renault, A. Kis, *npj 2D Mater. Appl.* **2018**, *2*, 12.

[19] T. Cao, Z. Li, S. G. Louie, *Phys. Rev. Lett.* **2015**, *114*, 236602.

[20] R. Longuinhos, J. Ribeiro-Soares, *Phys. Rev. Appl.* **2019**, *11*, 024012.

[21] Z. Zhu, Y. Cheng, U. Schwingenschlögl, *Phys. Rev. Lett.* **2012**, *108*, 266805.

[22] J. Guo, J.-J. Xie, D.-J. Li, G.-L. Yang, F. Chen, C.-R. Wang, L.-M. Zhang, Y. M. Andreev, K. A. Kokh, G. V. Lanskii, V. A. Svetlichnyi, *Light: Sci. Appl.* **2015**, *4*, e362.

[23] B. Jiang, Z. Hao, Y. Ji, Y. Hou, R. Yi, D. Mao, X. Gan, J. Zhao, *Light: Sci. Appl.* **2020**, *9*, 63.

[24] P. Tonndorf, S. Schwarz, J. Kern, I. Niehues, O. Del Pozo-Zamudio, A. I. Dmitriev, A. P. Bakhtinov, D. N. Borisenko, N. N. Kolesnikov, A. I. Tartakovskii, S. Michaelis de Vasconcellos, R. Bratschitsch, *2D Mater.* **2017**, *4*, 021010.

[25] D. J. Terry, V. Zólyomi, M. Hamer, A. V. Tyurnina, D. G. Hopkinson, A. M. Rakowski, S. J. Magorrian, N. Clark, Y. M. Andreev, O. Kazakova, K. Novoselov, S. J. Haigh, V. I. Fal'ko, R. Gorbachev, *2D Mater.* **2018**, *5*, 041009.

[26] M. Shiffa, B. T. Dewes, J. Bradford, N. D. Cottam, T. S. Cheng, C. J. Mellor, O. Makarovskiy, K. Rahman, J. N. O'Shea, P. H. Beton, S. V. Novikov, T. Ben, D. Gonzalez, J. Xie, L. Zhang, A. Patanè, *Small* **2024**, *20*, 2305865.

[27] J. Grzonka, M. S. Claro, A. Molina-Sánchez, P. J. F. S. Sadewasser, *Adv. Funct. Mater.* **2021**, *31*, 2104965.

[28] H. Nitta, T. Yonezawa, A. Fleurence, Y. Yamada-Takamura, T. Ozaki, *Phys. Rev. B: Condens. Matter Mater. Phys.* **2020**, *102*, 235407.

[29] Y. Zhang, Y.-W. Tan, H. L. Stormer, P. Kim, *Nature* **2005**, *438*, 201.

[30] T. J. B. M. Janssen, A. Tzalenchuk, S. Lara-Avila, S. Kubatkin, V. I. Fal'ko, *Rep. Prog. Phys.* **2013**, *76* 104501.

[31] C. Si, Z. Lin, J. Zhou, Z. Sun, *2D Mater.* **2016**, *4*, 015027.

[32] P. Deák, M. Han, M. Lorke, M. F. Tabriz, T. Frauenheim, *J. Phys.: Condens. Matter* **2020**, *32*, 285503.

[33] P.-F. Wang, Y. Liu, J. Yin, W. Ma, Z. Dong, W. Zhang, J.-L. Zhu, J.-L. Sun, *J. Mater. Chem.* **2019**, *7*, 887.

[34] N. T. Son, X. T. Trinh, L. S. Løvlie, B. G. Svensson, K. Kawahara, T. Suda, T. Kimoto, T. Umeda, J. Isoya, T. Makino, T. Ohshima, E. Janzén, *Phys. Rev. Lett.* **2012**, *109*, 187603.

[35] C. G. Hemmingsson, N. T. Son, E. Janzén, *Appl. Phys. Lett.* **1999**, *74*, 839.

[36] A. Rossi, D. Spirito, F. Bianco, S. Forti, F. Fabbri, H. Büch, A. Tredicucci, R. Krahne, C. Coletti, *Nanoscale* **2018**, *10*, 4332.

[37] S. Rehman, M. A. Khan, H. Kim, H. Patil, J. Aziz, K. D. Kadam, M. A. Rehman, M. Rabeel, A. Hao, K. Khan, S. Kim, J. Eom, D.-K. Kim, M. F. Khan, *Adv. Sci.* **2023**, *10*, 2205383.

[38] Q. Wang, W. Zhang, L. Wang, K. He, X. Ma, Q. Xue, *J. Phys.: Condens. Matter* **2013**, *25*, 095002.

[39] D. Nečas, P. Klapetek, *Open Phys.* **2012**, *10*, 181.

[40] P. Giannozzi, S. Baroni, N. Bonini, M. Calandra, R. Car, C. Cavazzoni, D. Ceresoli, G. L. Chiarotti, M. Cococcioni, I. Dabo, A. Dal Corso, S. de Gironcoli, S. Fabris, G. Fratesi, R. Gebauer, U. Gerstmann, C. Gougoussis, A. Kokalj, M. Lazzeri, L. Martin-Samos, N. Marzari, F. Mauri, R. Mazzarello, S. Paolini, A. Pasquarello, L. Paulatto, C. Sbraccia, S. Scandolo, G. Sclauzero, A. P. Seitsonen, et al., *J. Phys. Condens. Matter* **2009**, *21*, 395502.

[41] P. Giannozzi, O. Andreussi, T. Brumme, O. Bunau, M. Buongiorno Nardelli, M. Calandra, R. Car, C. Cavazzoni, D. Ceresoli, M. Cococcioni, N. Colonna, I. Carnimeo, A. Dal Corso, S. de Gironcoli, P. Delugas, R. A. DiStasio Jr., A. Ferretti, A. Floris, G. Fratesi, G. Fugallo, R. Gebauer, U. Gerstmann, F. Giustino, T. Gorni, J. Jia, M. Kawamura, H.-Y. Ko, A. Kokalj, E. Küçükbenli, M. Lazzeri, et al., *J. Phys. Condens. Matter* **2017**, *29*, 465901.

[42] J. P. Perdew, K. Burke, M. Ernzerhof, *Phys. Rev. Lett.* **1996**, *77*, 3865.

[43] T. Sohier, M. Calandra, F. Mauri, *Phys. Rev. B* **2017**, *96*, 075448.

[44] H. J. Monkhorst, J. D. Pack, *Phys. Rev. B* **1976**, *13*, 5188.

[45] S. Grimme, J. Antony, S. Ehrlich, H. Krieg, *J. Chem. Phys.* **2010**, *132*, 154104.

[46] D. G. A. Smith, L. A. Burns, K. Patkowski, C. D. Sherrill, *J. Phys. Chem. Lett.* **2016**, *7*, 2197.

[47] P. V. C. Medeiros, S. Stafström, J. Björk, *Phys. Rev. B* **2014**, *89*, 041407.

[48] P. V. C. Medeiros, S. S. Tsirkin, S. Stafström, J. Björk, *Phys. Rev. B* **2015**, *91*, 041116.

2404809 (10 of 10)